International Journal of Mechanical, Industrial and Aerospace Sciences
ISSN: 2517-9950
Vol:5, No:8, 2011

Numerical Analysis of Wind Loads on a Hemicylindrical Roof Building

Marco Raciti Castelli, Sergio Toniato and Ernesto Benini

***Abstract*—**The flow field over a three dimensional pole barn characterized by a cylindrical roof has been numerically investigated. Wind pressure and viscous loads acting on the agricultural building have been analyzed for several incoming wind directions, so as to evaluate the most critical load condition on the structure. A constant wind velocity profile, based on the maximum reference wind speed in the building site (peak gust speed worked out for 50 years return period) and on the local roughness coefficient, has been simulated.

In order to contemplate also the hazard due to potential air wedging between the stored hay and the lower part of the ceiling, the effect of a partial filling of the barn has been investigated.

The distribution of wind-induced loads on the structure have been determined, allowing a numerical quantification of the effect of wind direction on the induced stresses acting on a hemicylindrical roof.

***Keywords*—**CFD, wind, building, hemicylindrical roof.

I. Introduction and Background

CYLINDRICAL and curved roof buildings are increasingly adopted in modern agricultural architecture as they offer aerodynamically efficient shapes and provide designers with an alternative to rectangular building forms. Nevertheless, as observed by Blackmore et al. [1], there is little information available on the wind loads on cylindrical roofs. The proposed Eurocode for wind actions [2] includes pressure coefficients for a limited range of aspect ratio cylindrical roofs, obtained from experimental measurements in low-turbulence conditions, but only for wind blowing normal to the eaves. Some other national wind codes, such as the Australian and New Zealand code [3], the Canadian one [4] and the American (ASCE) one [5] provide only external pressure coefficients for curved roofs. Some other data are also reported by Cook [6] and Blackmore et al. [1].

The limitations in accurate pressure coefficient databases can be overcome by using advanced CFD (Computational Fluid Dynamic) codes, which can outflank the lack of experimental data thanks to their inherent ability to determine the aerodynamic components of actions through the integration of the Navier-Stokes equations in the neighborhood of the building. As observed by Raciti Castelli et al [7], the use of commercial CFD packages to calculate the wind flow and resulting action on civil structures has aroused a large credit both in research and academic communities as well as in consulting engineering societies, thanks to their capability of providing an insight into the flow field around the buildings even before their construction. Nevertheless, as observed by Blackmore et al. [1], the modeling of atmospheric turbulence, interacting with the structure-generated turbulent flow still depicts large difficulties that often lead to erroneous results when areas of flow separation are to be simulated. These problems have been discussed by several authors, including in particular Stathopoulos [8] [9], Timofeyef [10] and Ferreira et al. [11].

As pointed out by Stathopoulos [12], the flow around buildings is still extremely difficult to predict by computational methods, even for simple surrounding environments. However, there is increasing evidence that CFD-based techniques provide adequate responses in case the mean flow and pressure conditions are to be determined. Some of the specific design issues in the use of CFD for the prediction of flows around buildings were described by several authors:

- Yoshie et al. [14] performed comparative and parametric studies on the flow around a square prism, based on the work of Meng and Hibi [15], in order to validate CFD simulations of the absolute velocity field around high-rise buildings;
- Hak-Sun et al. [15] presented a numerical simulation of turbulent wind flow around a complex building using LES (Large Eddy Simulation). The numerical results were validated against the experimental measurements of a multi-block configuration of the WERFL (Wind Engineering Research Field Laboratory) building at Texas Tech University [16], showing good agreement;
- Raciti Castelli et al. [17] investigated the flow field over a flat roof model building, in order to assess CFD guidelines for the calculation of the turbulent flow over a structure immersed in an atmospheric boundary layer. To this purpose, a complete validation campaign was performed through a systematic comparison of numerical simulations and wind tunnel experimental data. Several

Marco Raciti Castelli is Research Associate at the Department of Mechanical Engineering of the University of Padua, Via Venezia 1, 35131 Padova, Italy and fluid dynamic specialist at ESPE S.r.l., Via Cappello 12/A, 35010 San Pietro in Gu (PD) (e-mail: marco.raciticastelli@unipd.it).

Sergio Toniato is Executive and Design Manager at ESPE S.r.l., Via Cappello 12/A, 35010 San Pietro in Gu (PD), Italy (e-mail: stoniato@espe.it).

Ernesto Benini is Associate Professor at the Department of Mechanical Engineering of the University of Padua, Via Venezia 1, 35131 Padova, Italy (e-mail: ernesto.benini@unipd.it).

turbulence models and spatial node distributions were tested, allowing a quantification of the capabilities of the CFD code to predict the flow separation and the extension of the recirculation regions downstream the building miniature.

Through the systematic application of these guidelines, the present work describes a full numerical campaign of simulations of the flow field around a three dimensional pole barn characterized by a hemicylindrical roof. Wind pressure and viscous loads acting on the building have been analyzed for several incoming wind directions (spaced 45° each other), so as to evaluate the most critical load condition on the structure. In order to contemplate also the hazard due to potential air wedging between the stored hay and the lower part of the ceiling, the effect of a partial filling of the barn has been investigated.

II. The Case Study

The present work is part of a research project finalized to the installation of a roof-based integrated photovoltaic system on top of a pole barn characterized by a hemicylindrical roof. Fig. 1 shows a picture of a typical pole barn for hay storage: as can be seen, it is composed of a cylindrical steel roof and two tympanums. It is constructed with special poles that serve as the underlying support structure for the outer walls and roof. The size of the pole shed can vary depending on the purposes it will be used for.

Fig. 1 Typical pole barn for hay storage

Some concerns came for the possible air wedging between the lower part of the ceiling and the stored hay, in case of a partial filling of the bar itself. For this reason a 75% filled pole bar was investigated for several incoming wind directions, so as to evaluate the most critical load condition on the structure.

III. Model Geometry

In the present work, the flow field around the pole barn was numerically simulated by reproducing a computational domain of rectangular shape, whose main geometrical features are summarized in Fig. 2 and Table 1.

As can be seen from Fig. 2, the model building was enclosed inside a cylindrical sub-domain, in order to rotate the structure around the vertical axis, thus allowing to evaluate the most critical load condition on the structure as a function of the angle α between the incoming wind direction and the pole barn longitudinal axis.

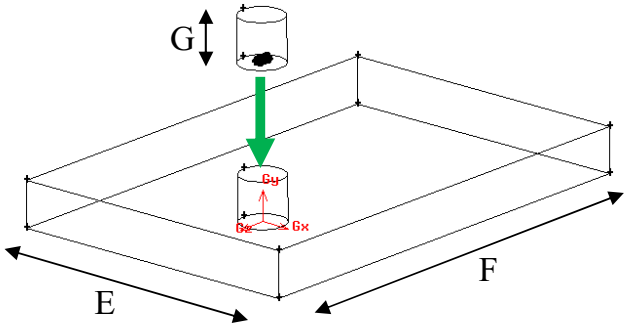

Fig. 2 Main geometrical features of the computational domain: the computational model allowed the rotation along the vertical axis (y) of the cylindrical sub-domain enclosing the building structure, in order to simulate several relative wind directions.

Table I
Main Dimensions of the Computational Domain

Denomination	Value [m]
Computational domain width, E	600
Computational domain length, F	900
Computational domain height, G	90
Cylindrical sub-domain diameter, D	90

The boundary conditions of the computational domain are reported in Fig. 3. A *Simmetry* boundary condition was adopted for the terrain, in order to avoid the development of an atmospheric boundary layer: this choice, though not realistic, allowed to invest the tested model with an uniform velocity profile, computed on the basis of the maximum reference wind speed in the building site (peak gust worked out for 50 years return period) and on the local roughness coefficient, as suggested by [18].

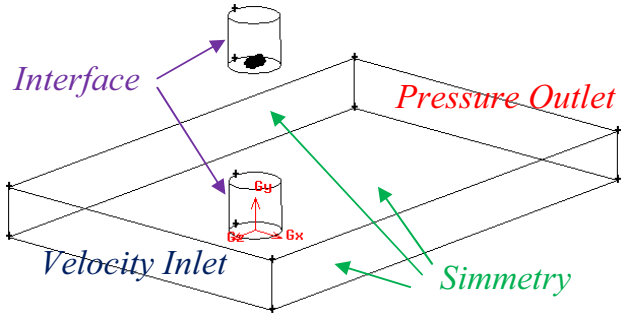

Fig. 3 Boundary conditions of the computational domain

Table 2 presents the main geometrical features of the analyzed pole barn, while Fig. 4 shows a vertical view of the

building structure, showing also the tympanum geometry. As can be seen, the shed does not end on the ground, in order to improve hay ventilation. Two lateral gutters are also visible.

TABLE II
MAIN GEOMETRICAL FEATURES OF THE ANALYZED POLE BARN

Denomination	Value [m]
Pole barn width, B	8.9
Pole barn length, L	30
Pole barn height, H	6.5
Tympanum height from the ground, h	4
Pole barn height from the ground, a	2
Lateral gutter width, b	0.7

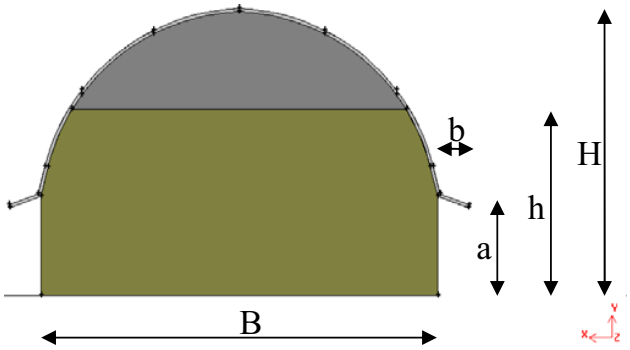

Fig. 4 Vertical view of the building, showing also the tympanum geometry (the hay is evidenced in brown).

Fig. 5 shows a 3D model of the building: for the sake of clarity, the pole barn longitudinal axis was initially oriented north-south, with the empty portion facing towards north (*Position 0°N*). It was successively rotated clockwise about the vertical axis (y), in order to analyze several relative wind directions, while the incoming wind remained from the north. The analyzed configurations are listed in Table 3.

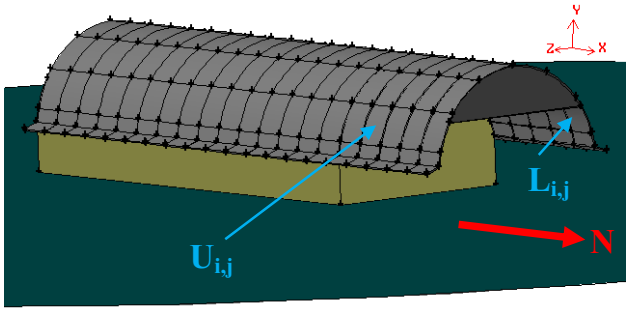

Fig. 5 Three dimensional model of the building (the hay is evidenced in brown), *Position 0°N*. A generical subsection $U_{i,j}$ of the upper roof portion is evidenced, as well as a generical subsection $L_{i,j}$ of the lower one.

In order to determine the distribution of wind-induced pressure and viscous loads on every portion of the structure, the hemicylindrical roof was subdivided into 400 subsections of different areas, 200 (10 width × 20 length) concerning the upper part and 200 (10 width × 20 length) concerning the corresponding lower one. This subdivision, visible in Fig. 5, allowed the calculation of two matrixes [10×20] containing the loads per unit area on every upper $[u_{i,j}]$ (or corresponding lower $[l_{i,j}]$) roof subsection, as exemplified in Fig. 6 for *Position 0°N*.

TABLE III
ANALYZED CONFIGURATIONS AS A FUNCTION OF THE ANGLE BETWEEN THE POLE BARN LONGITUDINAL AXIS AND THE INCOMING WIND DIRECTION

Configuration name	α [°]
Position 0°N	0
Position 45°N	45
Position 90°N	90
Position 135°N	135
Position 180°N	180

$$\begin{bmatrix} u_{20,1} & u_{20,2} & u_{20,3} & \dots & \dots & u_{20,8} & u_{20,9} & u_{20,10} \\ u_{19,1} & u_{19,2} & u_{19,3} & \dots & \dots & u_{19,8} & u_{19,9} & u_{19,10} \\ \dots & \dots & \dots & \dots & \dots & \dots & \dots & \dots \\ u_{1,1} & u_{1,2} & u_{1,3} & \dots & \dots & u_{1,8} & u_{1,9} & u_{1,10} \\ u_{1,1} & u_{1,2} & u_{1,3} & \dots & \dots & u_{1,8} & u_{1,9} & u_{1,10} \end{bmatrix}$$

N

Fig. 6 Exemplification of the [10×20] matrix containing the loads per unit area on every upper roof subsection, *Position 0°N*. The north direction is reproduced for the sake of clarity.

Through an algebraic sum of these two matrixes, the matrix containing the total loads per unit area $[t_{i,j}]$ on the roof of the building was determined, in formulas:

$$[t_{i,j}] = [u_{i,j}] + [l_{i,j}] \quad (1)$$

IV. SPATIAL DOMAIN DISCRETIZATION

An isotropic unstructured mesh was created around the model building. Considering their features of flexibility and adaption capability, unstructured meshes are in fact very easy to obtain, for complex geometries, too, and often represent the "first attempt" in order to get a quick response from the CFD in engineering work.

The spatial grid resolution adopted for the present calculations was based on the validation work performed by Raciti Castelli et al. [17]. In Table 4 the characteristic data of the adopted grid architecture are reported, as a function of the normalized grid resolution on the building, defined as:

$$Res_{building} = \Delta g_{building}/H \quad (2)$$

and as a function of the normalized grid resolution on outer computational domain, defined as:

$$Res_{domain} = \Delta g_{domain}/G \quad (3)$$

As a final step, the mesh elements have been fully converted into polyhedra. This option, applicable to unstructured grids of tetrahedral type, has the advantage of reducing the total number of grid elements, producing in the same time greater mesh regularity, as observed by Raciti Castelli and Benini [19].

TABLE IV
CHARACTERISTIC DATA OF THE ADOPTED GRID ARCHITECTURE

$Res_{building}$ [-]	Growth factor [-]	Res_{domain} [-]
0.01	1.15	0.11

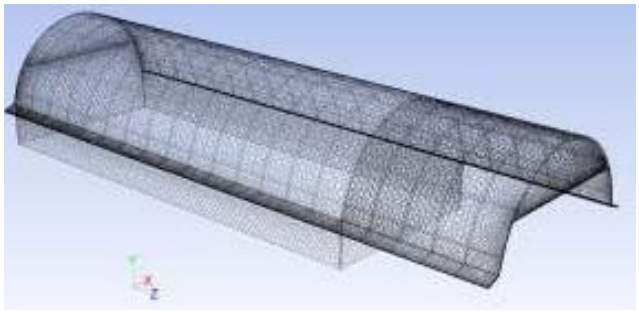

Fig. 7 Main geometrical features of the adopted grid refinement near the building

Fig. 8 Main geometrical features of the adopted grid inside the cylindrical sub-domain enclosing the building structure

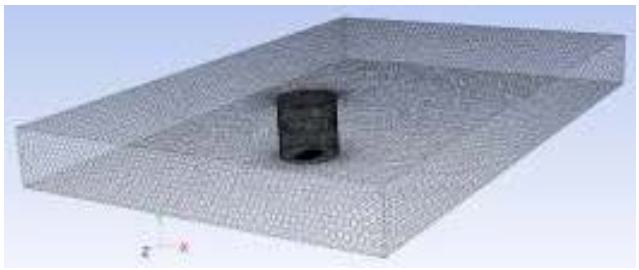

Fig. 9 Computational domain mesh

The conversion into polyhedra achieved a 60-70% reduction in the total element number. On the other hand, a polyhedral grid occupies the memory of a tetrahedral one almost twice. The total budget is therefore favorable to polyhedra, even considering the fact that a polyhedral mesh shows more marked regularity features than the corresponding tetrahedral one and therefore allows a much faster convergence. Figs. 7, 8 and 9 show the main features of the adopted grid. For further details upon the validation procedure, see [17].

TABLE V
MAIN COEFFICIENTS ADOPTED FOR THE CALCULATION OF THE MAXIMUM REFERENCE WIND SPEED

Denomination	Value
$v_{b,0}$(Zone 1) [m/s]	25
$v_{b,0}$(Zone 2) [m/s]	25
$v_{b,0}$(Zone 3) [m/s]	27
a_0(Zone 1) [m]	1000
a_0(Zone 2) [m]	750
a_0(Zone 3) [m]	500
a_s(Zone 1) [m]	1200
a_s(Zone 2) [m]	800
a_s(Zone 3) [m]	500
v_b [m/s]	27
c_t [-]	1
k_r [-]	0.19
z_0 [m]	0.05
z_{min}(Exposure Category II) [m]	4
$c_e(H)$ [-]	2.08
$v_{b,max}$ [m/s]	39.95

V. CALCULATION OF INLET WIND VELOCITY PROFILE

A constant velocity profile, based on the maximum reference wind speed in the building site (peak gust speed worked out for 50 years return period) was computed for Italian Zones No. 1, 2 and 3 and Exposure Category II [18]. After choosing the maximum allowed value for a_s and determining from [18] the values of $v_{b,0}$, a_0, k_a, c_t, k_r, z_0 and z_{min} for the building site, the reference wind speed was determined as:

$$v_b = v_{b,0} \quad \text{for:} \quad a_s \le a_0 \tag{4}$$

or:

$$v_b = v_{b,0} + k_a (a_s - a_0) \quad \text{for:} \quad a_0 < a_s \le 1500 \text{ m} \tag{5}$$

and the coefficient of exposure for the building site was determined as:

$$c_e(H) = k_r^2 \, c_t \ln(H/z_0)[7 + c_t \ln(H/z_0)] \tag{6}$$

being:

$$H \ge z_{min} \tag{7}$$

The maximum reference wind speed for the building site was eventually determined as:

$$v_{b,max} = [v_b^2 \, c_e(H)]^{0.5} \tag{8}$$

and resulted of 39.95 m/s. this value was adopted for all the presented numerical simulations.

Table 5 summarizes the main coefficients adopted for the calculation of the maximum reference wind speed.

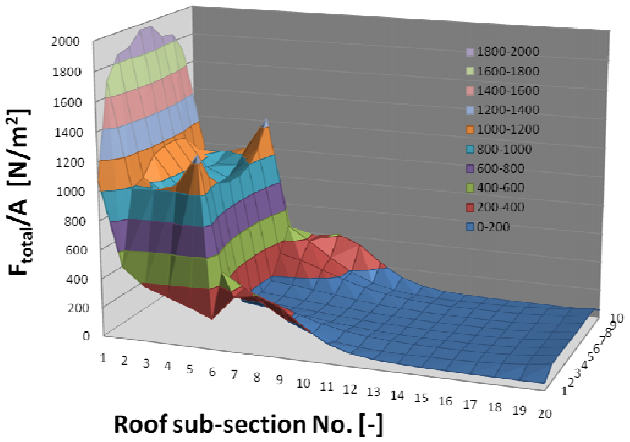

Fig. 10 Wind induced pressure and viscous loads on the pole barn roof, *Position 0°N*

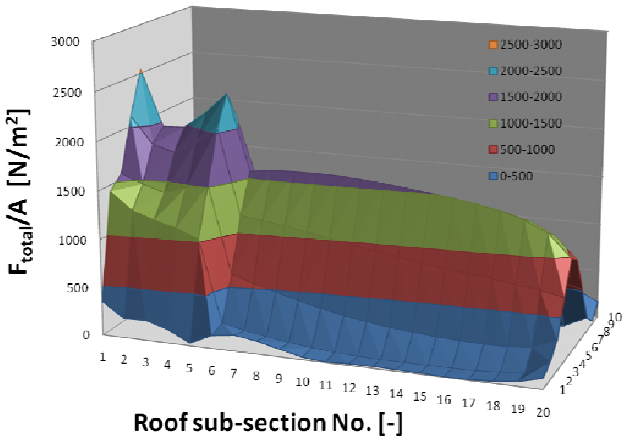

Fig. 11 Wind induced pressure and viscous loads on the pole barn roof, *Position 45°N*

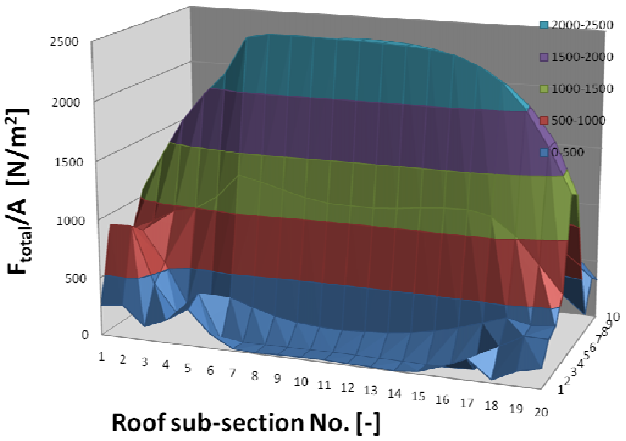

Fig. 12 Wind induced pressure and viscous loads on the pole barn roof, *Position 90°N*

VI. Turbulence Models and Convergence Criteria

Simulations were performed using the commercial RANS solver ANSYS FLUENT®, which implements 3-D Reynolds-averaged Navier-Stokes equations using a finite volume-finite element based solver. A segregated solver, implicit formulation, was chosen for unsteady flow computation. The fluid was assumed to be incompressible, being the maximum fluid velocity on the order of 70 m/s. Air density was set at 1.225 kg/m^3. Standard k-ε model was used for turbulent calculations, as suggested by [17].

As a global convergence criterion, residuals were set to 10-5. Each simulation, performed on a 8 processor, 2.33 GHz clock frequency computer, required a total CPU time of about 48 hours.

VII. Results and Discussion

Figs. from 10 to 14 show the distribution of wind-induced pressure and viscous loads on every portion of the roof for the five analyzed angles between the incoming wind direction and the pole barn longitudinal axis.

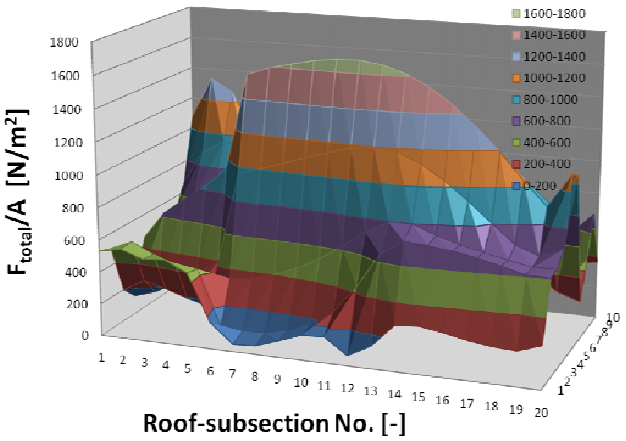

Fig. 13 Wind induced pressure and viscous loads on the pole barn roof, *Position 135°N*

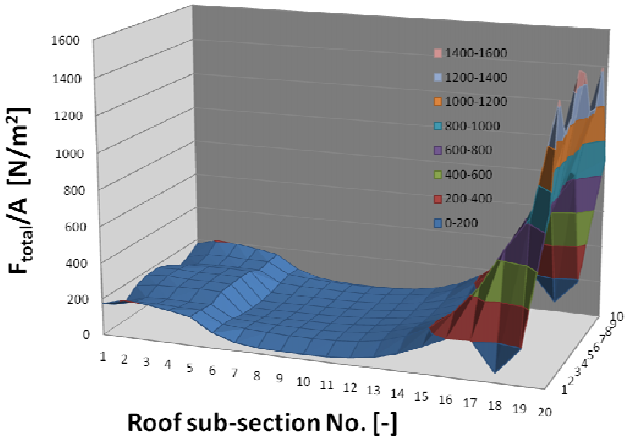

Fig. 14 Wind induced pressure and viscous loads on the pole barn roof, *Position 180°N*

As it can be clearly seen, the heaviest load condition is obtained for *Position 90°N*, that is for the wind blowing transversely with respect to the building longitudinal axis (two local force peaks are also visible for *Position 45°N*, but can be considered negligible if compared to *Position 90°N* global wind loads). As can be seen from Fig. 15, showing the contours of absolute velocity on a transversal section of the pole barn for *Position 90°N*, this fact is due to the geometry of the cylindrical roof, whose behavior is quite similar to an aerofoil for transversal wind, determining an acceleration of the flow in the whole upstream portion and a consequent lift force on the roof.

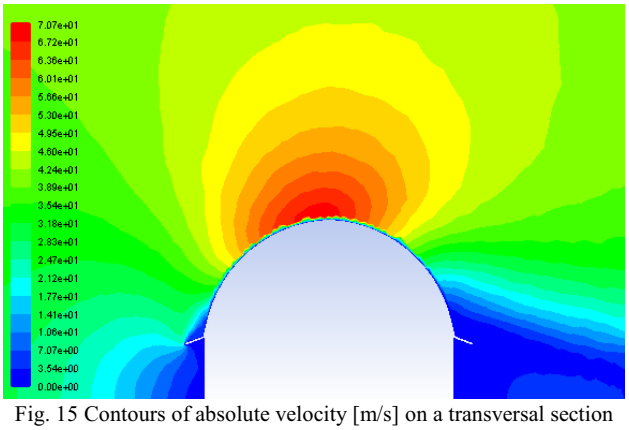

Fig. 15 Contours of absolute velocity [m/s] on a transversal section of the pole barn located in correspondence of roof sub-section No. 10, *Position 90°N*.

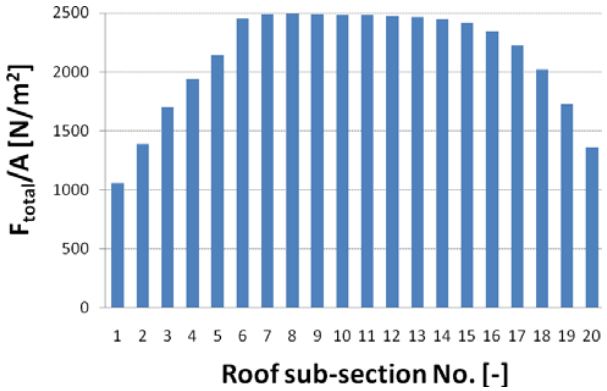

Fig. 16 Distribution of wind-induced total pressure and viscous loads along the longitudinal axis on top of the roof, *Position 90°N*. The load reduction due to side-effects is evidenced by the red circles.

Fig. 16 shows the distribution of wind-induced total pressure and viscous loads along the longitudinal axis on top of the roof, for *Position 90°N*. The load reduction due to side-effects is clearly visible: the most critical load condition is thus registered in the middle of the pole barn. It can also be noticed that the loads acting on the empty portion of the pole barn (left sub-sections from 1 to 5) are lower with respect to those acting on the corresponding portions on the right: this phenomenon is due to the down-force acting on the empty portion of the pole barn, due to the low-pressure area under the roof, as can be seen in Fig. 17. When the pole barn is full of hay, no down-force is able to counterbalance the uplift force acting on the upper portion of the roof, thus determining a higher wind-induced load, as can be seen from Fig. 18.

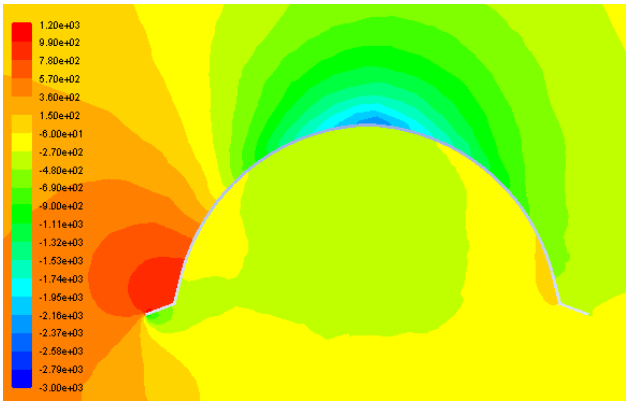

Fig. 17 Contours of static pressure [Pa] on a transversal section of the pole barns located in correspondence of roof sub-section No. 3, *Position 90°N*.

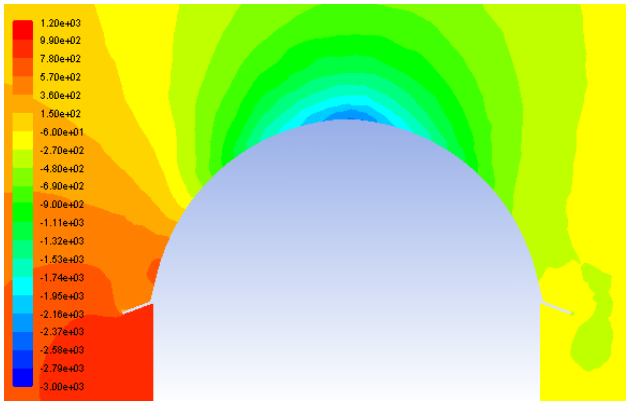

Fig. 18 Contours of static pressure [Pa] on a transversal section of the pole barns located in correspondence of roof sub-section No. 18, *Position 90°N*.

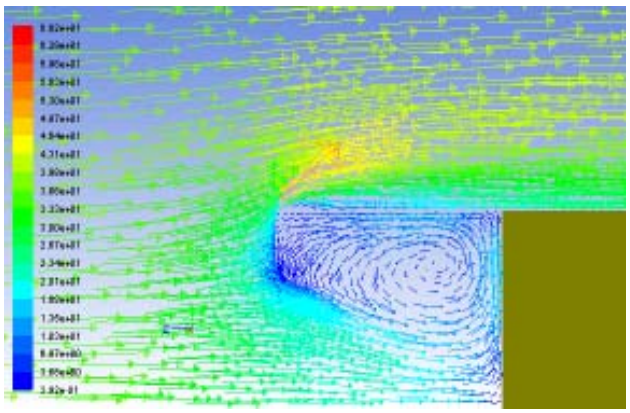

Fig. 19 Absolute velocity vectors [m/s] in the vertical plane parallel to the pole barn longitudinal axis, *Position 0°N*.

Finally, as can be clearly seen from Figs. 10 and 11, *Position 0°N* and *Position 45°N* registered a deep air wedging between the stored hay and the lower portion of the ceiling, causing a dramatic increase of wind-induced loads on the structure. This phenomenon can also be seen from Figs. 19 and 20, showing respectively the absolute velocity vectors in the vertical plane parallel to the pole barn longitudinal axis and the contours of static pressure for *Position 0°N*.

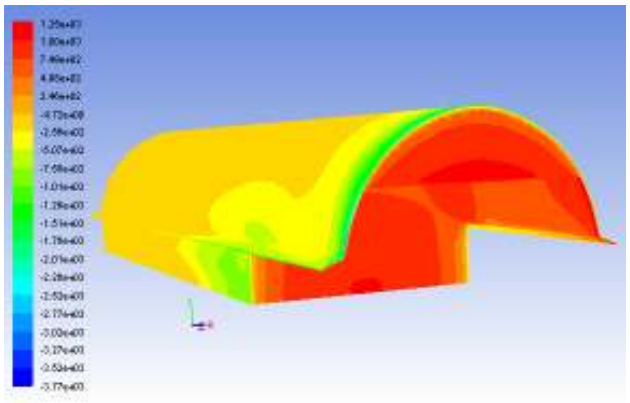

Fig. 20 Contours of static pressure [Pa], *Position 0°N*.

VIII. Conclusions and Future Works

A full numerical campaign of simulations of the flow field around a three dimensional pole barn characterized by a cylindrical roof was presented. Wind pressure and viscous loads acting on the building were analyzed for several incoming wind directions (spaced 45° each other), so as to evaluate the most critical load condition on the structure. In order to contemplate also the hazard due to potential air wedging between the stored hay and the lower part of the ceiling, the effect of a partial filling of the barn was investigated.

The heaviest load condition was obtained for the wind blowing transversely with respect to the building longitudinal axis. This phenomenon was ascribed to the geometry of the cylindrical roof, whose behavior is quite similar to an aerofoil for transversal wind, determining an acceleration of the flow in the whole upstream portion and a consequent lift force on the roof. Moreover, the load reduction due to side-effects was also registered: the most critical load condition was determined in the middle of the pole barn, allowing to perform a much simpler 2D simulation for future similar cases.

It was also noticed that the loads acting on the empty portion of the pole barn are lower with respect to those acting on the corresponding portions on the right: this phenomenon was ascribed to the down-force acting on the empty portion of the pole barn, due to the low-pressure area under the roof.

Finally, the simulations conducted for lower angles between the incoming wind direction and the pole barn longitudinal axis registered a deep air wedging between the stored hay and the lower portion of the ceiling, causing a dramatic increase of wind-induced loads on the structure. Further work should be done, in order to examine the effect of different pole barn filling on wind-induced pressure and viscous loads on the cylindrical roof.

Nomenclature

a [m]	pole barn height from the ground
a_0 [m]	reference height above sea level for the building site
a_s [m]	height of the building site above sea level
b [m]	lateral gutter width
B [m]	pole barn width
$c_e(H)$ [-]	coefficient of exposure for the building site and structure height
c_t [-]	coefficient of topography for the building site and height
D [m]	cylindrical sub-domain diameter
E [m]	computational domain width
F [m]	computational domain length
G [m]	computational domain height
h [m]	tympanum height from the ground
H [m]	pole barn height
k_r [-]	reference roughness coefficient at the building site
$l_{i,j}$ [N/m^2]	loads per unit area on a lower roof subsection

$[l_{i,j}]$	10×20 matrix containing the loads per unit area on every lower roof subsection
L [m]	pole barn length
$L_{i,j}$ [-]	generical subsection of the lower roof portion
$Res_{building}$ [-]	normalized grid resolution on the building
Res_{domain} [-]	normalized grid resolution on outer computational domain
$[t_{i,j}]$	10×20 matrix containing the total loads per unit area on every roof subsection
$u_{i,j}$ [N/m^2]	loads per unit area on an upper roof subsection
$[u_{i,j}]$	10×20 matrix containing the loads per unit area on every upper roof subsection
$U_{i,j}$ [-]	generical subsection of the upper roof portion
v_b [m/s]	basic wind speed at the building site and height above sea level
$v_{b,0}$ [m/s]	basic wind speed at the building site
$v_{b,max}$ [m/s]	maximum reference wind speed at the building site
z_0 [m]	reference height of roughness coefficient for the building site
z_{min} [m]	minimum reference height of roughness coefficient for the building site
α [°]	angle between the incoming wind direction and the pole barn longitudinal axis
$\Delta g_{building}$ [m]	grid resolution on the building
Δg_{domain} [m]	grid resolution on outer computational domain
ρ [kg/m^3]	air density (set at 1.225 kg/m^3)

ACKNOWLEDGMENT

The present work was performed in cooperation with E.S.P.E. S.r.l., San Pietro in Gu (Italy) as part of a research project finalized to the installation of a roof-based integrated photovoltaic system on top of a pole barn characterized by a cylindrical roof.

REFERENCES

[1] P. A. Blackmore, E. Tsokri, G. Breeze, "Wind Loads on Cylindrical Roofs", *Proceedings of the International Conference on Urban Wind Engineering and Building Aerodynamics*, COST Action C14, Von Karman Institute, Rhode-Saint-Genèse, Belgium May 5-7, 2004.

[2] prEN1991-1-4, *Eurocode 1*: "Action on Structures – Part 1-4: General Actions – Wind Actions", Stage 49 draft, Jan 2004.

[3] Australian/New Zealand Standard, *Structural design actions*, "Part 2: wind actions", AS/NZS 1170.2:2002, June 2002.

[4] User's Guide – "NBC 1995 Structural commentaries (Part 4)", NRC/CNRC, *Canadian Commission on Building and Fire Codes*, National Research Council of Canada, April 2002.

[5] ASCE Standard, "Minimum design loads for buildings and other structures", *ANSI/ASCE 7-95*, American Society of Civil Engineers, June 1996.

[6] N. J. Cook, "*The designers guide to wind loading of building structures*", Part 2, Butterworths, 1995.

[7] M. Raciti Castelli, S. Toniato, E. Benini, "Numerical Analysis of Wind Induced Pressure Loads on an Integrated Roof-Based Photovoltaic System", MAS 2011, *The 10th International Conference on Modeling and Applied Simulation*, 12-14 September 2011, Rome, Italy.

[8] T. Stathopoulos, "The numerical wind tunnel for industrial aerodynamics: real or virtual in the new millennium?", *Wind and Structures*, 2002.

[9] T. Stathopoulos, A Baskaran, "Computational simulation of wind environmental conditions around buildings", *Engineering Structures*, Vol. 18, 876-885, 1996.

[10] N. Timofeyef, "Numerical study of wind mode of a territory development", *Proceedings of the 2nd East Europe Conference on Wind Engineering*, Prague, Czech Rep., 1998.

[11] A. D. Ferreira, D. X. Viegas, A. C. Sousa, "Numerical and experimental study of the wind flow around a group of low-rise buildings", *Proceedings of the 10th International Conference on Wind Engineering*, Copenhagen, Denmark, 1999.

[12] T. Stathopoulos, "Wind Effects on People", *Proceedings of the International Conference on Urban Wind Engineering and Building Aerodynamics*, COST Action C14, Von Karman Institute, Rhode-Saint-Genèse, Belgium, May 5-7, 2004.

[13] R. Yoshie, A. Mochida, T. Tominaga, H. Kataoka, K. Harimoto, T. Nozu, T. Shirasawa, "Cooperative project for CFD prediction of pedestrian wind environment in the Architectural Institute of Japan", *Journal of Wind Engineering and Industrial Aerodynamics*, 95 (2007), pp. 1551-1578.

[14] Y. Meng, K. Hibi, "Turbulent measurements of the flow field around a high-rise building", *J. Wind Eng. Jpn.* (76), pp. 55-64, 1998.

[15] K. Hak-Sun, L. Sungsu, C. Gulgi, "Numerical Simulation of Wind around Building Complex", Proceedings of the Seventh Asia-Pacific Conference on Wind Engineering, Nov. 8-12, 2009, Taipei, Taiwan.

[16] C. H. Chang, R. N. Meroney, "Concentration and flow distributions in urban street canyons: wind tunnel and computational data", *Journal of Wind Engineering and Industrial Aerodynamics*, 91 (2003), pp. 1141-1154.

[17] M. Raciti Castelli, A. Castelli, E. Benini, "Modeling Strategy and Numerical Validation of the Turbulent Flow over a two-Dimensional Flat Roof", World Academy of Science, Engineering and Technology, Vol. 79 (2011).

[18] DM 14/01/2008 – "Norme tecniche per le costruzioni", issued on the Italian *Gazzetta Ufficiale* on February 4, 2008.

[19] M. Raciti Castelli, E. Benini, "Effect of Blade Inclination Angle on a Darrieus Wind Turbine", Journal of Turbomachinery, May 2012, Vol. 134, 031016.